

Article

Distribution of Trace Elements (Ag, Pd, Cd, and Mn) between Pyrite and Pyrrhotite and Selectivity of Surficial Nonautonomous Phases in a Hydrothermal System

Sergey Lipko , Vladimir Tauson , Nikolay Smagunov , Dmitriy Babkin and Irina Parkhomenko

A.P.Vinogradov Institute of Geochemistry, Siberian Branch of Russian Academy of Sciences, Favorskiy Str. 1A, 664033 Irkutsk, Russia

* Correspondence: slipko@yandex.ru; Tel.: +7-3952-42-99-67

Abstract: The dual distribution coefficients (D) that are related to structurally and superficially bound trace element (TE) in pyrite (Py) and pyrrhotite (Po) associations, crystallized hydrothermally at 400 °C and 1 kbar pressure, were determined. Three independent methods were used to estimate the structural and surficial TE contents (C^{str} and C^{sur}) and the corresponding D Py/Po values (D^{str} and D^{sur}), which were found, on average, to be 12.4, 0.8, 0.9, and 0.06 (D^{str}) and 2.6, 0.7, 2.0, and 0.07 (D^{sur}) for Ag, Pd, Cd, and Mn, respectively. The coincidence of a dual D for several elements was a result of coupled changes in C^{sur} and C^{str} . The selectivity (S) of the surficial nonautonomous phases (NAPs) that were responsible for TE accumulation (which is the ratio of TE concentrations in surficial and structural modes) was determined. It was shown that the interpretation of TE uptake by surficial phases was adequate and that this phenomenon is common in nature, independently of the system where it occurs—i.e., in experimental autoclaves or in hydrothermal ore deposits. Studies of NAPs selectivity can help in evaluating the total element compatibility in minerals and the maximum possible contents of structurally bound admixtures of the element (solubility) in minerals under given conditions. A significant surficial impurity accumulation effect is most important and well-pronounced for incompatible micro-elements with concentrations of less than ~0.1 wt%. The surficial mode may be a source of Pd and other platinum group elements and more abundant and easily refined than the structurally bound mode.

Keywords: pyrite; pyrrhotite; trace elements; distribution coefficients; structurally and surficially bound modes; nonautonomous phases; selectivity; hydrothermal system



Citation: Lipko, S.; Tauson, V.; Smagunov, N.; Babkin, D.; Parkhomenko, I. Distribution of Trace Elements (Ag, Pd, Cd, and Mn) between Pyrite and Pyrrhotite and Selectivity of Surficial Nonautonomous Phases in a Hydrothermal System. *Minerals* **2022**, *12*, 1165. <https://doi.org/10.3390/min12091165>

Academic Editor: Jan Marten Huizenga

Received: 21 August 2022

Accepted: 11 September 2022

Published: 15 September 2022

Publisher's Note: MDPI stays neutral with regard to jurisdictional claims in published maps and institutional affiliations.



Copyright: © 2022 by the authors. Licensee MDPI, Basel, Switzerland. This article is an open access article distributed under the terms and conditions of the Creative Commons Attribution (CC BY) license (<https://creativecommons.org/licenses/by/4.0/>).

1. Introduction

The pyrite–pyrrhotite equilibrium is a buffer reaction that determines sulfur activity in ore systems, thereby regulating the behavior of elements hosted in S-bearing complexes. Despite the widespread occurrence of this mineral association in different types of deposits, trace element (TE) partitioning in the pyrite–pyrrhotite pair has not been extensively studied experimentally. The mineral formation parameters may be evaluated if the distribution coefficients of trace elements (TEs) between pyrite and pyrrhotite ($D_{TE}^{Py/Po}$) are determined. This is supported, for example, by the temperature dependences of $D_{TE}^{Py/Po}$ for Ni and Co [1]. However, it is known that temperature and pressure are not the only parameters that affect the interphase distribution of TEs; other factors may also be important [2]. In the case of pyrite–pyrrhotite associations, the stress-related properties of the minerals appear to be significant, due to the more ductile behavior of pyrrhotite relative to pyrite and, therefore, the development of deformation defects and low- and high-angle dislocation boundaries in pyrrhotite crystals [3].

Trace elements can be incorporated differently into such intracrystalline boundaries, which, for their part, exhibit a selectivity with respect to particular TEs. For instance, the

element profiles of Pb, Bi, and Ag in pyrrhotite crystals associated with pyrite demonstrate a close relationship with high- and low-angle boundaries, where their concentrations are commonly higher than those of Co and As [3]. The interrelations between individual crystals in pyrite–pyrrhotite associations are commonly complicated, due to phase transformations under varying T and fS_2 parameters during processes of ore metamorphism [4], producing highly developed intercrystalline interfaces and the enrichment in specific TEs.

The most common two-dimensional defect of the structure of a real crystal appears to be its surface. Indeed, this defect can concentrate TEs through both their adsorption and the formation of a surficial nonautonomous phase (NAP) during the crystal growth process under conditions involving the “external” (forced) supersaturation of growth media in hydrothermal systems, where traditional physical adsorption and chemisorption processes are less effective [5]. Studies by photoemission electron microscopy and X-ray magnetic circular dichroism have previously revealed the presence of non-magnetic inclusions at the surface of pyrrhotite crystals interpreted as pyrite [6]. However, it seems likely that, as an alternative to mechanical contamination with pyrite, the relicts of the pyrite-like NAP may have formed in accordance with the principle of the continuity of NAP formation on the surfaces of coexisting minerals [7]. Evidently, the external surfaces, as well as the intracrystalline boundaries, can uptake selected TEs; simple logic suggests that the enrichment of crystals’ surfaces with TEs relative to the volume element contents characterizes the elements that are poorly accommodated in the structure of the host crystals. In magmatic systems, pyrite can be formed through the decomposition of a S-rich monosulfide solid solution (MSS) at temperatures below 740 °C, but typically, pyrite occurs as a product of post-magmatic sulfidization or the oxidation of MSS and its exsolution products—pentlandite and pyrrhotite.

The study of TE distribution allows us to obtain information about post-magmatic metamorphic and hydrothermal events. Thus, analysis of the co-localization of elements shows that the remobilization of TEs during the substitution of pyrrhotite with pyrite can lead to a decrease in these element concentrations relative to those of the parent pyrrhotite. Indicators of such processes include impurity elements, such as Mn, Ag, and Pb [8], although Pb is not usually considered a significant structural admixture of iron sulfides. Instead of Pb, an impurity element reflecting the contribution of hydrothermal fluids to the mineral forming process may be Cd, whose speciation in pyrrhotite has previously been studied in detail by experimental methods [9]. In contrast, platinum group elements (PGEs), represented in this article by Pd, are possible indicators of mineral formation from primary sulfide liquids.

The typomorphic properties of TEs can only be interpreted if the distribution coefficients of the latter are known at different stages of the mineral formation process. In the present work, these coefficients were determined for hydrothermal conditions using diverse methods for the differentiation of structurally and superficially bound modes of TE occurrences. The partitioning of elements in the structural mode was determined by the physicochemical conditions of the system. The surficial mode (NAP) characterized the growth medium and mechanisms of formation of the crystals, and their capacity for selective TE uptake. These observations have practical importance in light of the formation of so-called hidden metal-rich features, which does not occur in readily determined forms, such as proper mineral phase TE inclusions and increased TE contents in bulk crystals [10].

2. Methods

2.1. Experimental Procedure and Obtained Phases

The pyrite–pyrrhotite association was produced using standard techniques of hydrothermal thermogradient synthesis [10] in a 212 cm³-sized stainless-steel autoclave equipped with a Ti alloy (VT-8) passivated insert with a volume of 63 cm³. The temperature in the zone of crystal growth was 400 °C and the pressure was 100 MPa (1 kbar), according to the PTFC diagram of a mineralizing solution containing 10 wt% NH₄Cl [11]. The full duration of the experiment was 30 days, with the application of an isothermal regime

during the first five days to homogenize the batch material and ensure near-equilibrium conditions for the subsequent 25 days of thermogradient crystallization, with a temperature drop of 20 °C on the exterior wall of the autoclave. The experiment was terminated with autoclave quenching under cold running water, with a temperature drop of 5 °C/s. The experimental system was organized in a way that allowed compatible quantities of pyrite and pyrrhotite to be obtained. The 7.09 g batch contained (wt%) Fe (42.9), S (29.6), Mn_2O_3 (24.2), CdS (2.0), Ag (1.0), and Pd (0.3). The mole ratio S/Fe was 1.2, and that of Mn_2O_3 /Fe was 0.2. The batch consisted of domestically produced reagents of high chemical purity (pure reagent-grade).

The crystals of magnetic pyrrhotite formed more or less isometric hexagonal prisms and elongated hexagonal pyramids, often with high *l*-index faces (Figure 1). The pyrite crystals formed cubes commonly complicated by {111} and rarely by {110} and {hk0} faces. The crystal sizes of both minerals mainly ranged from ~0.5 to 1.5 mm along an edge. X-ray diffraction (XRD) analyses of the pyrrhotite composition, using interplanar spacing (102), revealed an Fe content of 46.4 at%.



Figure 1. Crystals of associated pyrite and pyrrhotite displaying a prevailing crystal habit (synthesis conditions—400 °C, 1 kbar, 10 % NH_4Cl solution).

2.2. Analytical Methods

Atomic absorption spectrometry (AAS) succeeded by analytical data selections for single crystals (ADSSC) can provide unique data on TE speciation through the separation of structural and surficial binding forms. The ADSSC procedure has previously been described in detail [10,12,13]. It is based on the rank-scale statistical sampling of analytical data for individual TE-containing crystals and accounts for the properties of TE uptake by mineral crystals. A comparison with independent methods has demonstrated the possibility of determining the contents of structural impurities of elements with an uncertainty of ± 30 rel% [10,13,14]. Additional details regarding data processing with the ADSSC procedure in the particular case of the pyrite and pyrrhotite crystals are provided below (Section 3.1). The AAS measurements were performed on PerkinElmer devices (Model 503 and Analyst 800, PerkinElmer Corp., Branford, CT, USA).

Laser ablation inductively coupled plasma mass spectrometry (LA-ICP-MS) was used as an independent method to obtain information on TE speciation and the distribution of TEs using two approaches [15]. The first approach involved analyses of polished crystal sections pressed into epoxy cartridges; the results obtained refer to the volume contents of TEs. In the second approach, native crystal faces were analyzed to determine the TE concentrations in surficial layers of crystals (≤ 20 μm , [15]). Two standard samples were used here: the glass sample NIST 612 from the National Institute of Standards and Technology, and the in-house standard material consisting of greenockite (α -CdS) single crystals synthesized

hydrothermally and containing 76.1 wt% Cd, 21.2 wt% S, 1.0 wt% Fe, 1.7 wt% Se, 150 µg/g Pd, 420 µg/g Pt, 460 µg/g Ag, 170 µg/g As, and 580 µg/g Mn. The isotopes measured were ^{105}Pd , ^{55}Mn , ^{111}Cd , ^{112}Cd , ^{107}Ag , and ^{109}Ag . Measurements were performed on an Agilent 7500 ce unit manufactured by Agilent Technologies with a quadrupole mass analyzer (Agilent Tech., Santa Clara, CA, USA), using a New Wave Research UP-213 ablation platform. The parameters of the LA-ICP-MS experiment were (figures in parentheses refer to polished crystals): a plasma power of 1580 (1400) W, carrier gas flow rate of 1.5 (1.2) L/min, plasma-forming gas flow rate of 15 L/min, cooling gas at 1 L/min, laser energy at 100% (80%), wavelength 213 nm, frequency of 20 Hz, a laser spot diameter of 100 (55) µm, dwell times per isotope/element of 0.15 (0.25) s, and acquisition times of 30 (25) s. Measurements were made on 15 to 20 points in several (4 or 5) crystals from each sample of pyrite and pyrrhotite. The calculated minimum detection limits (MDL) for Pd amounted to 1.55 µg/g and 0.45 µg/g for native surfaces and polished crystals, respectively. The other TEs were relatively abundant (≥ 26 µg/g) and their MDLs were not determined.

Information about Cd speciation was obtained using element thermo-release atomic absorption spectrometry (ETR-AAS), i.e., AAS with a temperature control of element release from the sample [9,16]. The method applicable to relatively volatile elements is based on a simultaneous registration of the temperature of a sample and the absorbance signal from the spectrometer. In this study, this method was applicable to Cd only, but we considered it useful for the reliability verification of all methods used. The temperature of release of the element from the sample depended on the binding form of this element in the mineral. The temperature of maximum release was the characteristic of the bond strength in a particular mode and could be estimated from the calibration of the method with synthetic minerals with well-defined element species. A schematic design of the analytical device is presented in [16]. A Perkin–Elmer Model 503 atomic absorption spectrometer equipped with a deuterium background corrector and Perkin–Elmer HGA graphite furnaces was used. The sample was held in a Pt boat. The sample boat was positioned in the furnace very close to the hotspot of the Pt–Pt/Rh thermocouple. The furnace was operated under argon flow. The uncertainty in the temperature of maximum Cd release was no more than $\pm 5\%$. The detection limit for Cd was 0.3 ng, and the precision was ± 20 – 30 rel%, depending on the separation and reproducibility of peaks of the elements' thermo-release (so-called thermopeaks). The quantitative analysis was performed using the procedure of deconvolution of a smoothed curve of the element release. To minimize errors, we used the in-house standard sample of hydrothermally synthesized galena crystals containing 0.02 wt% Cd in a structural mode and an optimal heating rate preset with a heating program regulator.

3. Results

3.1. Trace Element Contents and Distribution Coefficients

3.1.1. Atomic Absorption Spectrometry—Analytical Data Selections for Single Crystals

Following the ADSSC procedure, we used euhedral crystals of different sizes with clean, faultless faces (as available). Preference was given to pyrite cubes and nearly isometric pyrrhotite prisms that could be approximated by a parallelepiped. Proceeding from the average crystal size to the specific surface area of the average crystal in size fraction required information on the form coefficient k for a crystal shape approximated by a true polyhedron [10]. Each crystal belonging to particular size fraction was weighted on an analytical microbalance and transferred into beakers for dissolution and subsequent TE determination by AAS. The obtained data were processed statistically by dividing the dataset into the intervals of crystal masses (sizes), where the following average parameters were determined: the crystal mass in every size fraction (\bar{m}), the length of the true polyhedron edge (\bar{r}), the specific surface area (\bar{S}_{sp}), and the TE concentration (\bar{C}_{TE}) (see Table 1).

Table 1. Results of the AAS–ADSSC analysis of single crystal size selections of coexisting pyrite and pyrrhotite obtained in hydrothermal system at 400 °C and 1 kbar.

Mineral	Number of Cryst. (Starting-Final Sample)	Characteristics of the Final Sample						TE Contents **			
		Num. of Cryst.	Range of Mass. (mg)	\bar{m} (mg)	\bar{r} (mm)	\bar{S}_{sp} (mm ² /mg)	$\bar{C}_{TE \pm \epsilon}$ (µg/g)*	\bar{C}^{-tot}	\bar{C}^{-ev}	C^{str}	\bar{C}^{-sur}
Ag, µg/g 10⁻²											
Pyrite	40–27	7	0.24–0.77	0.47	0.455	2.643	56.7 ± 17.9	27.4	21.3	4.3	17.0
		7	0.81–1.37	1.07	0.598	2.005	34.1 ± 9.3				
		6	1.48–1.82	1.70	0.698	1.720	22.2 ± 5.5				
		7	2.10–8.41	4.61	0.973	1.232	14.4 ± 4.1				
Pyrrhotite	63–38	6	0.25–0.65	0.56	0.493	2.604	31.2 ± 18.9	28.3	9.9	0.36	9.4
		7	0.72–1.01	0.91	0.581	2.226	32.0 ± 10.1				
		5	1.03–1.48	1.29	0.652	1.977	15.9 ± 10.5				
		8	1.51–1.86	1.73	0.719	1.793	7.8 ± 1.9				
		5	1.87–2.51	2.33	0.794	1.623	4.3 ± 1.2				
		7	2.54–5.80	4.59	0.996	1.297	4.7 ± 1.4				
Pd, µg/g											
Pyrite	40–28	6	0.24–0.77	0.60	0.493	2.431	95 ± 32	32	28	1.6	26
		7	0.81–1.32	0.99	0.583	2.060	55 ± 9				
		8	1.36–1.82	1.69	0.697	1.725	30 ± 4				
		7	2.10–8.41	4.54	0.968	1.238	13 ± 3				
Pyrrhotite	54–41	9	0.25–0.72	0.54	0.488	2.646	110 ± 25	36	32	1.6	32
		7	0.80–1.01	0.93	0.585	2.208	45 ± 13				
		9	1.03–0.94	1.30	0.654	1.974	38 ± 6				
		9	1.58–1.87	1.72	0.718	1.798	36 ± 4				
		7	1.92–5.80	3.81	0.936	1.380	13 ± 5				
Cd, µg/g 10⁻²											
Pyrite	40–22	6	0.24–0.77	0.55	0.479	2.503	9.4 ± 5.9	11.3	3.4	0.5	2.8
		5	0.81–1.37	1.06	0.596	2.011	3.8 ± 2.4				
		5	1.48–1.82	1.72	0.701	1.714	5.6 ± 4.5				
		6	2.10–8.41	4.72	0.981	1.223	1.8 ± 1.2				
Pyrrhotite	63–40	8	0.25–0.65	0.51	0.479	2.699	0.42 ± 0.12	1.09	0.33	n/d	
		6	0.72–1.01	0.89	0.576	2.237	0.40 ± 0.23				
		5	1.03–1.48	1.33	0.659	1.959	0.31 ± 0.13				
		8	1.51–1.86	1.70	0.715	1.804	0.41 ± 0.16				
		7	1.87–2.51	2.20	0.779	1.655	0.45 ± 0.21				
		6	2.54–5.80	4.25	0.970	1.328	0.22 ± 0.12				
Mn, µg/g 10⁻²											
Pyrite	40–25	5	0.24–0.77	0.52	0.470	2.549	10.8 ± 6.5	12.1	7.1	3.04	3.8
		8	0.81–1.37	1.10	0.604	1.990	8.4 ± 1.8				
		5	1.48–1.82	1.72	0.701	1.714	10.6 ± 5.2				
		7	2.10–8.41	4.26	0.948	1.266	4.9 ± 1.4				
Pyrrhotite	63–56	10	0.25–0.65	0.53	0.485	2.663	41.5 ± 4.0	40.9	40.2	n/d	
		10	0.72–1.01	0.89	0.576	2.237	39.7 ± 1.6				
		9	1.03–1.48	1.21	0.638	2.018	38.8 ± 4.2				
		11	1.51–1.86	1.70	0.715	1.804	40.9 ± 3.7				
		8	1.87–2.51	2.16	0.775	1.668	39.8 ± 1.4				
		8	2.54–5.80	4.38	0.980	1.316	40.4 ± 1.2				

* Errors (ε) were calculated as $\epsilon = t_{\alpha n} \cdot S_x / \sqrt{n}$ at a confidence level of 0.95, where $t_{\alpha n}$ is the Student’s coefficient for n degrees of freedom and S_x is the rms deviation. ** \bar{C}^{-tot} is the average total content; \bar{C}^{-ev} is the evenly distributed TE content for all size fractions; C^{str} is the structurally bound form concentration (\bar{S}_{sp} extrapolation to zero); \bar{C}^{-sur} is the average superficially bound form concentration. Cd and Mn in pyrrhotite exhibited the lack of concentration-size dependence and, therefore, the ADSSC method could not differentiate structurally and superficially bound forms; n/d indicates "not determined".

Table 1 shows that the number of crystals with evenly distributed TEs ranged from 22 to 28 for pyrite grains and from 38 to 56 for pyrrhotite. This was mainly due to the lack of coarse pyrite crystals of adequate quality. Thereafter, we constructed the dependences $\bar{C}_{TE} = f(\bar{S}_{sp})$, best approximated with an exponent (Figures 2 and 3). The extrapolation of these curves to a zero-specific surface provided the bulk TE contents, which were identified in our model [10] with structurally bound TE contents (C^{str}). The superficially bound TE contents (C^{sur}) characterized an average crystal among all size samplings—that is, the surface-related excess concentration of the element—and could be calculated with the equation provided in [10]. In this formula, the amount of a TE substance was normalized to the whole average crystal, providing the possibility of comparing the contributions of each

mode of TE to the TEs total concentration. The results of C^{str} and C^{sur} determination and the corresponding TE distribution coefficients between coexisting pyrite and pyrrhotite are shown in Table 2.

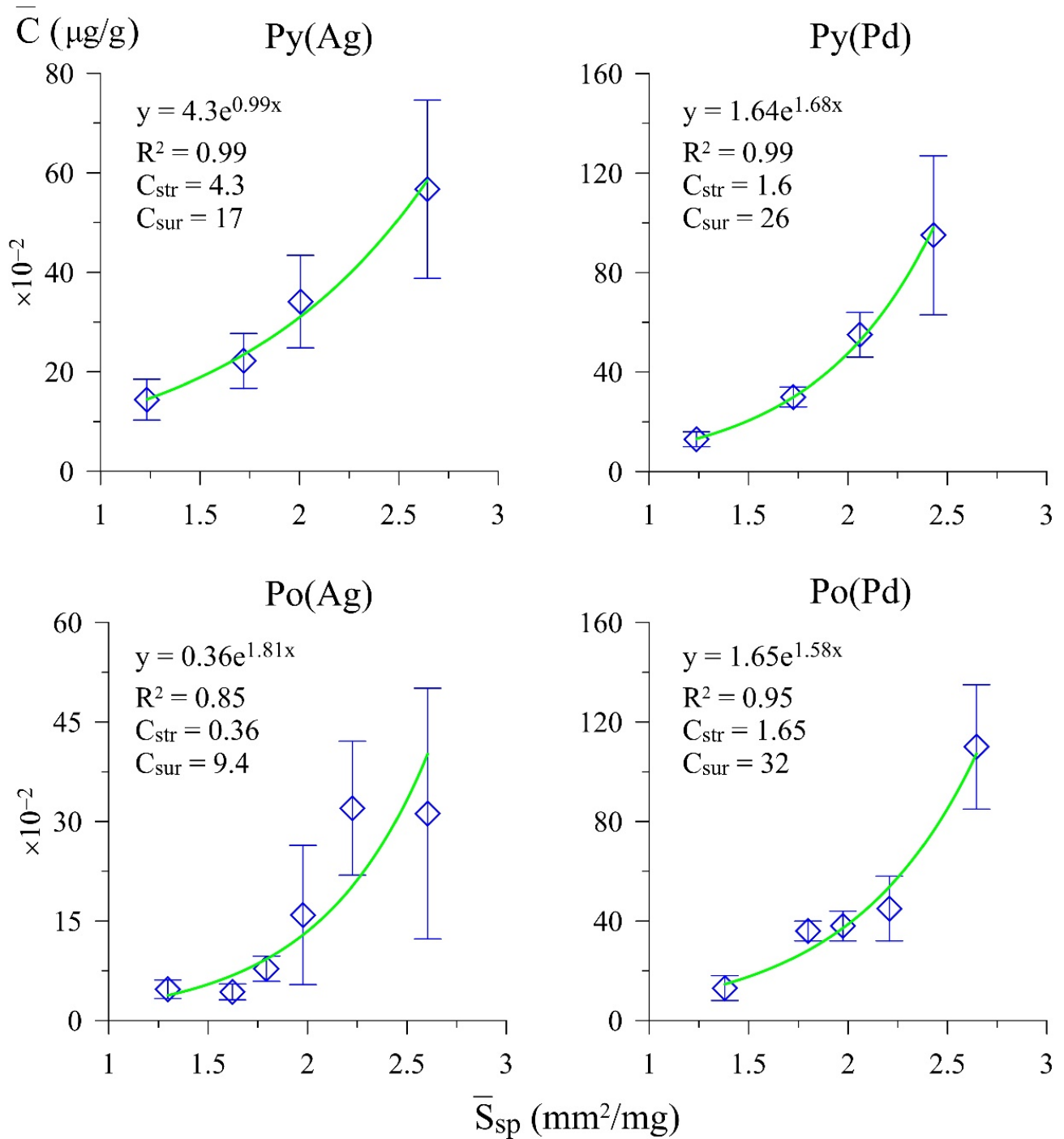


Figure 2. Dependence of the average concentrations of evenly distributed TEs in pyrite (Py) and pyrrhotite (Po) on the specific surface area of an average crystal of crystal-size fractions. The expressions for the approximate curves and concentrations of structurally and superficially bound modes are shown (see Table 1 for details).

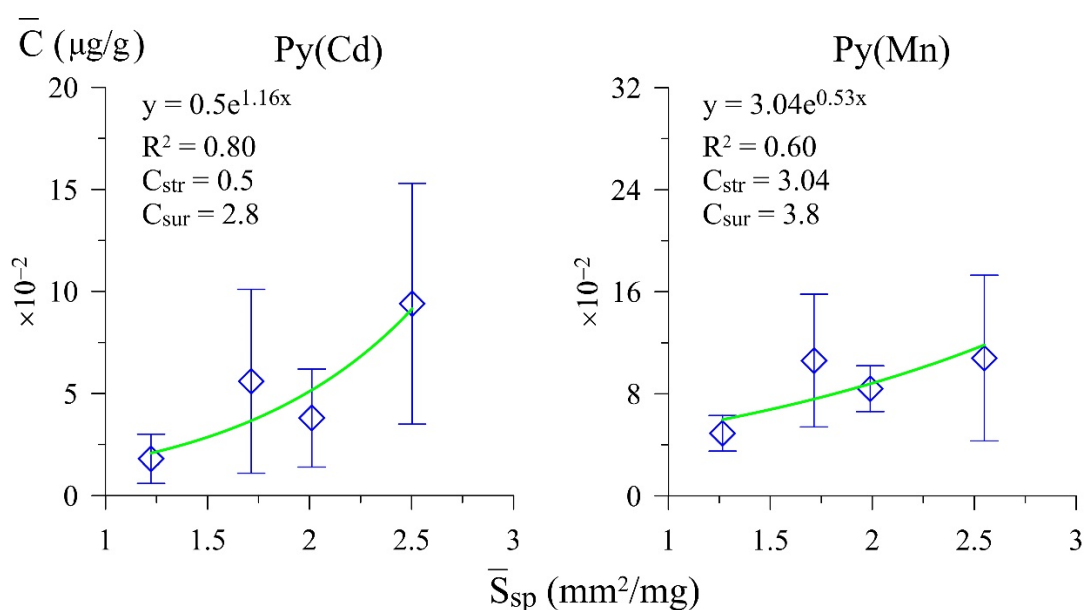


Figure 3. Dependence of the average concentrations of evenly distributed Cd and Mn in pyrite on the specific surface area of an average crystal of crystal-size fractions. See Figure 2 for explanations.

Table 2. Ag, Pd, Cd, and Mn contents and distribution coefficients (in terms of weight and atomic values) in the pair pyrite–pyrrhotite at 400 °C and 1 kbar from the data of AAS–ADSSC analysis.

Element	Pyrite				Pyrrhotite				$D_{Py/Po}^{str}$		$D_{Py/Po}^{sur}$	
	C^{str}		C^{-sur}		C^{str}		C^{-sur}		wt	at	wt	at
	μg/g	at%	μg/g	at%	μg/g	at%	μg/g	at%				
Ag	430	$1.59 \cdot 10^{-2}$	1700	$6.31 \cdot 10^{-2}$	36	$1.44 \cdot 10^{-3}$	940	$3.76 \cdot 10^{-2}$	11.9	11	1.8	1.7
Pd	1.6	$6.01 \cdot 10^{-5}$	26	$9.77 \cdot 10^{-4}$	1.6	$6.48 \cdot 10^{-5}$	32	$1.3 \cdot 10^{-3}$	1	0.9	0.8	0.8
Cd	50	$1.78 \cdot 10^{-3}$	280	$9.96 \cdot 10^{-3}$	33	$1.26 \cdot 10^{-3}$	n/d *		1.5	1.4	n/d	
Mn	304	$2.21 \cdot 10^{-2}$	380	$2.77 \cdot 10^{-2}$	4020	0.315	n/d		0.08	0.07	n/d	

* n/d indicates not determined; see Table 1.

It should be noted that the coefficients of determination of the dependences presented in Figure 2 are quite high, which supports the approach presented here and in our previous studies [10,14]. However, the size dependences of Cd and Mn in pyrrhotite remain unknown. Table 2 shows that structural Ag strongly fractionates into pyrite, whereas Mn fractionates into pyrrhotite (Py/Po distribution coefficients of 11 and 0.07, respectively; hereafter, we use atomic concentrations of TEs, if not specifically stipulated). The structural modes of Pd and Cd demonstrate slight and diverse fractionation ($D^{str} = 0.9$ and 1.4, respectively; hereafter, we omit the Py/Po index for convenience). The NAP-assistant surficially bound Ag slightly fractionates into pyrite ($D^{sur} = 1.7$), whereas the Pd surficial mode negligibly prefers pyrrhotite ($D^{sur} = 0.8$).

3.1.2. Laser Ablation Inductively Coupled Plasma Mass Spectrometry

Table 3 shows the TE contents determined for polished crystal sections (volume content) and native crystal faces (surficial layers). The data on C^{vol} were identified with C^{str} because we used the same procedure of data set “purification” as in the ADSSC data processing [10,14]. The results obtained support the data presented above for the preferential accumulation Ag structurally bound by pyrite relative to pyrrhotite ($D^{vol} = D^{str} = 13.9$). The structural modes of Pd and Cd slightly preferred pyrrhotite ($D^{str} = 0.7$ and 0.6, respectively); Mn strongly preferred pyrrhotite in both the structural and

surficial modes ($D^{str} = 0.06$, $D^{sur} = 0.07$). The surficial modes of Pd and Cd demonstrated a diverse behavior which was, however, not conspicuous ($D^{sur} = 0.6$ and 1.8, respectively).

Table 3. Element contents in the volume of crystal and in near-surface regions (within $\sim 20 \mu\text{m}$) of pyrite and pyrrhotite crystals from LA-ICP-MS data, and volume and surficial distribution coefficients.

Element	Pyrite				Pyrrhotite				$D_{Py/Po}^{vol}$		$D_{Py/Po}^{sur}$	
	C^{vol}		C^{sur}		C^{vol}		C^{sur}		wt	at	wt	at
	$\mu\text{g/g}$	at%	$\mu\text{g/g}$	at%	$\mu\text{g/g}$	at%	$\mu\text{g/g}$	at%				
Ag	390	$1.45 \cdot 10^{-2}$	750	$2.78 \cdot 10^{-2}$	26	$1.04 \cdot 10^{-3}$	200	$7.99 \cdot 10^{-3}$	15	13.9	3.8	3.5
Pd	0.8	$3 \cdot 10^{-5}$	12	$4.51 \cdot 10^{-4}$	1.1	$4.46 \cdot 10^{-5}$	20	$8.1 \cdot 10^{-4}$	0.7	0.7	0.6	0.6
Cd	29	$1.03 \cdot 10^{-3}$	230	$8.18 \cdot 10^{-3}$	45	$1.73 \cdot 10^{-3}$	120	$4.6 \cdot 10^{-3}$	0.6	0.6	1.9	1.8
Mn	290	$2.11 \cdot 10^{-2}$	350	$2.55 \cdot 10^{-2}$	4200	0.329	4440	0.348	0.07	0.06	0.08	0.07

3.1.3. Element Thermo-Release Atomic Absorption Spectrometry and Comparison of Methods

Figure 4 shows an example of the thermopeaks of Cd release during the study of pyrite and pyrrhotite powdered crystals with the ETR–AAS method [9,16].

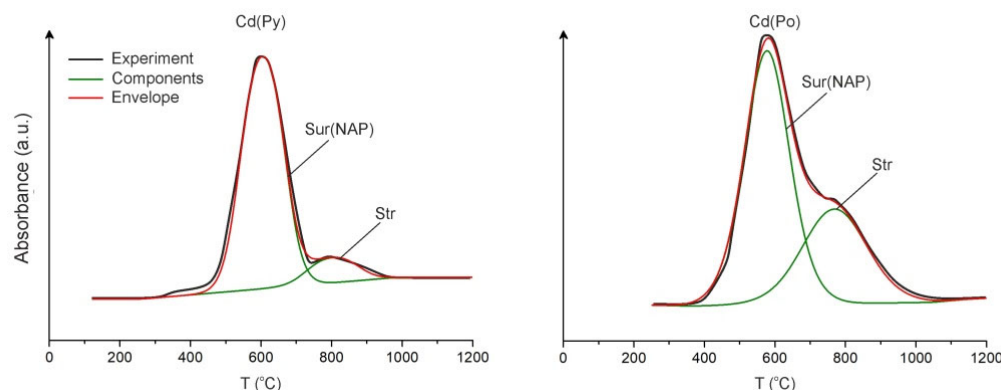


Figure 4. Absorbance–temperature curves of Cd release from pyrite (Py) and pyrrhotite (Po) samples. The NAP-related surficial mode with a maximum release temperature T_m of $\sim 600 \text{ }^\circ\text{C}$ dominates over the structural mode with $T_m \sim 800 \text{ }^\circ\text{C}$.

The quantitative data are provided in Table 4 alongside a comparison with Cd contents determined via the methods described above.

Table 4. Comparison of the results of Cd modes determined by different methods.

Method	Mode and Concentration of Cd, $\mu\text{g/g}$					
	Structural		Surficial		Str/Sur	
	Py	Po	Py	Po	Py	Po
AAS–ADSSC	50	33	280	n/d	0.18	n/d
LA-ICP-MS	29	45	230	120	0.13	0.38
ETR–AAS	32	50	290	140	0.11	0.36

The ETR–AAS data showed that Cd fractionated into a surficial mode (NAP) in both phases, but highly so in pyrite (on average, the structural-to-surficial mode ratios were 0.14 and 0.37 for pyrite and pyrrhotite, respectively). The comparison of the different methods of Cd speciation analysis allowed us to estimate the accuracy of TE mode determination as $\pm 20\text{--}40 \text{ rel}\%$. Therefore, the data obtained could be qualified as semiquantitative [14].

The average D^{str} and D^{sur} values (Tables 2–4) were 12.4, 0.8, 0.9, and 0.06 (D^{str}) and 2.6, 0.7, 2.0, and 0.07 (D^{sur}) for Ag, Pd, Cd, and Mn, respectively. The data for Pd, Cd, and

Mn may prompt an illusion of D constancy, but the coincidence of dual D in some cases was a result of coupled changes in C^{sur} and C^{str} [10].

3.2. Selectivity of NAPs for Trace Elements

Table 5 summarizes the data obtained with respect to NAP selectivity regarding the TEs studied.

Table 5. Selectivity (S) of surficial nonautonomous phases of pyrite and pyrrhotite to the trace elements studied.

Method	Mineral	Element	S^*
AAS-ADSSC	Pyrite	Ag	4.0
		Pd	16.2
		Cd	5.6
		Mn	1.2
	Pyrrhotite	Ag	26.1
		Pd	20.0
		Ag	1.9
		Pd	15.0
LA-ICP-MS	Pyrite	Cd	7.9
		Mn	1.2
	Pyrrhotite	Ag	7.7
		Pd	18.2
		Cd	2.7
		Mn	1.1
ETR-AAS	Pyrite	Cd	9.1
	Pyrrhotite	Cd	2.8

* $S = C_{sur}/C_{str}$.

The selectivity (S) was defined as the ratio of the element contents in surficial and structural modes. A relatively high selectivity was observed for Ag in pyrrhotite, Cd in pyrite, and Pd in both minerals. The reasons for such a behavior of the TEs studied is discussed in the next section. The data on S values for noble metals in pyrite, presented in Table 6, were compared with previously obtained data for Ag [17].

Table 6. Selectivity of pyrite NAP to Ag and Pd, according to experimental data.

Element	S	Experimental Conditions	Source of Data
Ag	5.2	500 °C, 1 kbar, NH ₄ Cl-based solutions, growth rate ~0.03–0.09 mm/day	Reference [17]
	10.4		
	8.7		
	3.6		
Ag	3.0 *	400 °C, 1 kbar, 10% NH ₄ Cl, growth rate ~0.02–0.04 mm/day	This work
Pd	15.6 *	The same	This work

* Average of AAS-ADSSC and LA-ICP-MS data.

One can see that at higher temperatures (500 °C) and slightly faster growth rates, the S values were systematically higher. This may have been due to the better development of the NAP during a greater oversaturation of the growth medium [10,17].

4. Discussion

4.1. Systems and Trace Element Speciation

4.1.1. Fe-S-Ag

Early “dry” experiments [18] with mixtures of Ag₂S and FeS₂ heated at 600 °C and 500 °C for 74 and 167 days, respectively, demonstrated that the solubility of Ag in FeS₂ was less than 0.1 at%. The solubility of Ag in pyrrhotites of various compositions was

determined to be less than 0.1 at% Ag at 600 °C (after 58 days of an “appearance-of-phase” experiment [18]). Recent “dry” experiments in the system Fe–S–Au–Ag confirmed the absence of miscibility between FeS₂ and Ag at 500 °C [19]. It was demonstrated that the solubility of Ag in pyrite and pyrrhotite at 500 °C was less than 0.03 wt% Ag, which was the sensitivity limit of X-ray spectral microanalysis; measurable contents were only obtained for troilite (0.079 ± 0.016 wt% Ag [20]). Hydrothermal Ag-bearing pyrite prepared at 500 °C and 1 kbar [17] was studied by various methods (AAS–ADSSC, SEM–EDX, AFM, EMPA) and the results obtained suggested that the solid solution of Ag in pyrite was unstable (i.e., it could not be quenched), and the limit of Ag accommodation in FeS₂ at 500 °C could be estimated at 0.09 ± 0.06 wt%. Despite large uncertainties, this value did not contradict the present result of 0.04 wt% Ag in structural form obtained at 400 °C (Tables 2 and 3). The structurally bound Ag fractionated strongly into pyrite in this mineral pair, in contrast to the superficially bound form, which only slightly preferred pyrite. The high selectivity of pyrrhotite NAP with respect to Ag may have been related to the surficial phase composition correlation and the presence of pyrite-like NAP on the surface of coexisting pyrrhotite crystals [7]. Regarding the very low solubility of Ag in bulk pyrrhotite [18], such an effect can provide a relatively high *S* value, as shown in Table 5 (17 for a mean of two methods). For pyrite, *S* = 3.0 on average at 400 °C (Table 6) and higher values were obtained at 500 °C (3.6 to 10.4), possibly due to a higher *T* gradient for growth and, therefore, a better NAP development according to the previously proposed mechanism of NAP formation [5,10].

4.1.2. Fe–S–Pd

The incorporation limit of Pd into pyrrhotite in the system Fe–Pd–S strongly depends on sulfur fugacity and the temperature of the system [21,22]. The maximum solubilities of Pd in pyrite and pyrrhotite determined through “dry” experiments were investigated by [21] using EPMA analyses, revealing the following solubility values (at% Pd): 0.04 and 2.0 at 725 °C, 0.04 and 0.30 at 550 °C, and 0.15 and 0.09 at 400 °C for pyrite and pyrrhotite, respectively. The data from Table 1 in [21] related to the pyrite–pyrrhotite association were combined with our data at 400 °C and were used for plotting the dependence shown in Figure 5: $\ln D_{Pd}^{Py/Po} = 8106/T - 11.75$, where *T* in K, *R*² = 0.89.

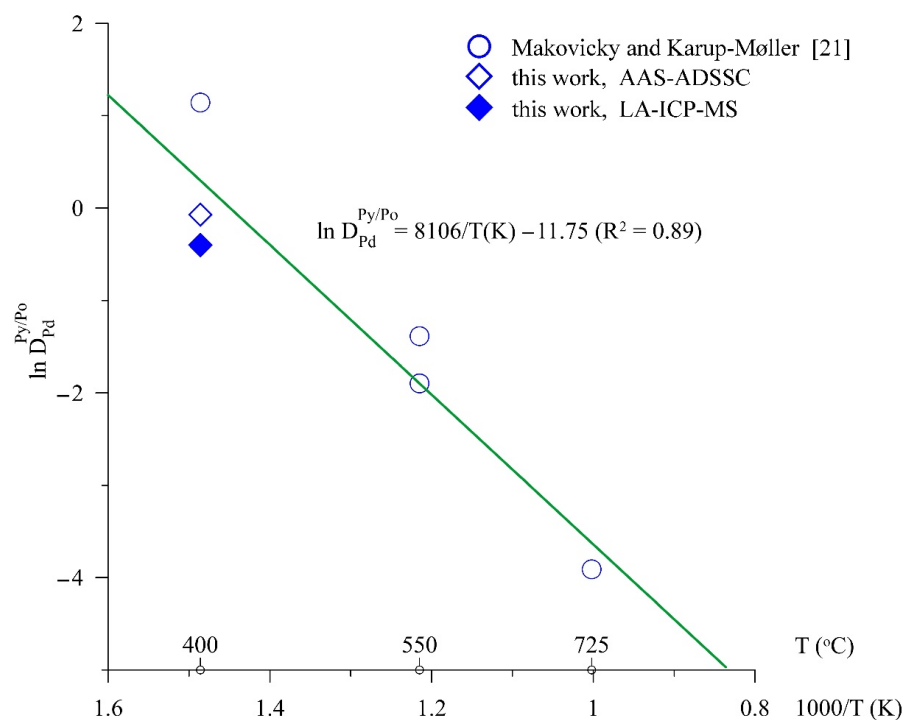


Figure 5. Palladium distribution coefficient between pyrite and pyrrhotite as a function of temperature.

It is interesting to note that at $T < \sim 420$ °C, D_{Pd} becomes >1 and Pd begins to preferentially partition into pyrite over pyrrhotite. This is an important observation that could help to distinguish primary (high-temperature) pyrite–pyrrhotite associations from secondary ones. Although the closure temperature for pyrrhotite is expected to be low (<100 °C, [22]), the primary composition may be reconstructed based on the character of Pd distribution and ADSSC procedure [14,17], as Pd contents are usually much lower than the Pd saturation limit. Palladium demonstrates a high and nearly equal NAP selectivity during the crystallization of both pyrite and pyrrhotite in hydrothermal systems (Table 5). Relative to other elements in this study, Pd was far from reaching saturation in the bulk of the crystals. The dualistic distribution coefficient [10,17] suggests the preferential incorporation of Pd into surficial NAP relative to the bulk. In such a case, the differences between NAPs, in composition and structure, on pyrite and pyrrhotite crystals appear to be insignificant in affecting the S value. However, they should be important in determining the fractionation of Pd and other PGEs in hydrothermal sulfide ores [23].

4.1.3. Fe–S–Cd

Considering the speciation of Cd in pyrrhotite, the effect of stoichiometric vacancies having maximal concentrations in pyrrhotite during its equilibrium with pyrite should be contemplated. Cadmium solubility in pyrrhotite has previously been determined at 700 °C and 600 °C under different sulfur fugacities [9]. The discrimination between Cd modes was undertaken using ETR–AAS (see Section 2.2). The maximum Cd concentrations were determined as 0.018 and 0.01 at% Cd at 700 °C and 600 °C, respectively. The evaluation of the interaction parameter Q of a regular solid solution $(Fe,Cd)_{1-x}S$ from these data is relatively simple. Such calculations provided values of 64 and 62 kJ/mol at 700 °C and 600 °C, respectively (average 63 ± 1), demonstrating the validity of the regular model. Using the determined Q parameter, the Cd solubility in pyrrhotite at 400 °C was evaluated using the following equation (valid for $x \ll 1$): $\ln x = -Q/RT$, where x is the mole fraction of CdS, R is the gas constant, and T represents the temperature in K. The value obtained ($6.5 \cdot 10^{-4}$ at% Cd) was somewhat lower than what was determined for the Cd structural mode (Tables 2–4). At 450 °C and a 1 kbar pressure in association with pyrite, magnetite, and greenockite, pyrrhotite contained 12 µg/g to 19 µg/g Cd or $(4.6$ to $7.3) \cdot 10^{-4}$ at% Cd [13]. Calculations with $Q = 63$ kJ/mol provided a value of $1.4 \cdot 10^{-3}$ at% Cd, which was slightly higher and close to the values obtained in this work (Tables 2 and 3). In association with pyrrhotite, magnetite, and greenockite at 450 °C and 1 kbar, pyrite contained 31 µg/g to 50 µg/g Cd [13], in reasonable agreement with the results of the present work (29 µg/g to 50 µg/g, Table 4). This proves that the system was saturated in CdS, although greenockite crystals were not observed in the considered pyrite–pyrrhotite association. Independently of the reason for some discrepancy, it is worth noting that the conditions of our experiment at 400 °C were close to saturation of pyrrhotite and pyrite in cadmium. Under these conditions, the surficial modes were significant. However, the ratios of structural to surficial modes were obviously lower for pyrite (Table 4), and the NAP selectivity differed by ~ 3 times in favor of pyrite (Table 5). One possible reason was a better development of NAPs on the surface of the pyrite crystals (see the AFM and XPS data in [13]).

4.1.4. Fe–S–Mn

Iron sulfide can contain up to 3.3 mol% MnS at 400 °C (extrapolation of data provided in [24] for 600 °C). In a ternary association of pyrite–pyrrhotite–magnetite, $Fe_{1-x}S$ was saturated to 0.63 ± 0.02 wt% Mn at 450 °C and 1 kbar, and Mn was homogeneously distributed throughout the crystals supporting the structural character of the impurity [13]. Therefore, 0.4 wt% Mn (Tables 2 and 3) corresponds to a structural mode of Mn; the surficial enrichment is low, and the S value is only 1.1 (Table 5). Therefore, in pyrrhotite, Mn is a compatible element in the bulk crystal; the AAS–ADSSC method did not reveal a size dependence of its concentration (Table 1). Manganese contents in the bulk crystal were relatively high and evenly distributed; therefore, the contribution of the

surficial form to the total content was negligible. The situation with Mn in pyrite is somewhat controversial. Experiments on the aforementioned ternary association [13] have exposed the size dependence of Mn concentrations in pyrite at relatively low total contents (0.15 wt%) and, in fact, its structurally bound mode was estimated as 0.008 wt% Mn using AAS–ADSSC analysis. However, in the experiment considering higher Mn bulk contents in pyrite (0.51 wt%), this dependence was not reproduced, and Mn was present at concentrations of 0.3 wt%, independently of the average crystal specific surface. The total Mn concentration in pyrite in the present study was 0.12 wt% (Table 1); 0.03 wt% of this was present in structural mode (Tables 2 and 3). The NAP selectivity of 1.2 (Table 5) is higher than that for Mn in pyrrhotite, where this impurity obviously corresponded to the structural mode.

4.2. NAP Selectivity: Comparison of Experimental and Natural Data

The surficial enrichment of minerals with TEs in ore systems was determined only for several noble metals in pyrite crystals [10,23,25]. However, a comparison of natural and experimental data appeared to be important, because it can shed light on the mechanism, rate, and practical significance of the phenomenon. The natural data supported the high variability of Ag fractionation and *S* values, even within a single deposit (Table 7).

Table 7. NAP selectivity to Ag and Pd for pyrites of several orogenic gold deposits (Magadan region, Northeastern Russia).

Deposit	Sample no.	<i>S</i> *		Reference
		Ag	Pd	
Natalkinskoe	Nat-10	18.3	4.5	[23]
The same	UV-3/13	1.8	18.4	"
"	TPM-1/1	n/d	15.6	[25]
"	M-161/10	"	11.9	"
Degdekan	DG-10/14	1.7	6.8	[23]
"	M-163/10	n/d	7.5	[10]
Zolotaya Rechka	ZR-10/13	6.4	9.4	[23]

* Determined by the AAS–ADSSC method. " indicates "the same"

As shown above, this may have been due to the ambiguous status of Ag admixtures in pyrite and the possible exsolution of Ag during post-crystallization events. In contrast to Ag, Pd demonstrated a stable behavior at a level of $S = 10.6 \pm 5$ (rmsd) (Table 7). This value was in reasonable agreement (within rms deviation) with the experimental results (Table 6) and we can infer that our interpretation of the TE uptake by surficial phases [5,10,25] is adequate and that this phenomenon is common in nature, independently of the system where it occurs (i.e., in experimental autoclave settings or within hydrothermal ore deposits).

5. Conclusions

The pyrite–pyrrhotite association synthesized at 400 °C and 1 kbar in an experimental hydrothermal system demonstrated dualism in the distribution of TEs (Ag, Pd, Cd, and Mn) related to surficial NAPs, which can uptake additional amounts of elements relative to their structural mode counterparts. The selectivity of NAPs with respect to TEs and the ratio of TE contents in surficial and structural modes depend on the character of the admixed elements and the growth conditions defining the development, structure, and composition of the surficial phases. The *S* values were low for elements capable of being incorporated into the sulfide mineral structures as true isomorphic admixtures or defect-assistant structural impurities (Mn and Cd in pyrrhotite, respectively). The surficial impurity accumulation effect was most important at low concentrations ($\leq \sim 0.1\%$) for incompatible TEs (Pd and Cd in pyrite, Pd and Ag in pyrrhotite). Among the elements studied in this work, Pd and Cd in pyrite and Pd and Ag in pyrrhotite were undoubtedly among the elements oversaturating the matrices in pyrite–pyrrhotite pairs. A differentiation of the structural and surficial

modes at a level of micro-concentration is required to study of mineral typomorphism, because it allows primary and secondary geochemical environments to be distinguished using TE indicators. The logarithm D^{str} Pd demonstrated a linear dependence on $1/T$, allowing a distinction to be made between high- and low-temperature associations. The natural data for pyrite of gold ore deposits supported a high variability of both Ag fractionation and S values within a single deposit, which may have been due to the ambiguous status of Ag admixtures in pyrite and the possible exsolution of Ag during post-crystallization events. In contrast to Ag, Pd demonstrated a stable behavior that was in reasonable agreement with the experimental results. Indeed, we can infer that our interpretation of the TE uptake by surficial phases [5,10,25] is adequate and that this phenomenon is common in nature and, therefore, must be considered in ore evaluation and the planning of ore-processing activities. Evaluating the structurally bound mode of TEs can help determine the T, P conditions of mineral formation. Studies of NAP selectivity can help in evaluating the total element compatibility in minerals and the maximum possible contents of structurally bound admixtures of specific elements (their solubility) in minerals under given conditions. The fractionation of impurities into NAPs over the solubility limit provides a clear rise to the selectivity over ~ 1.1 , the value characterizing a wide isomorphic miscibility (e.g., Mn in pyrrhotite). The NAP selectivity for Pd corresponded to the selectivity determined for pyrites of gold ore deposits of northeastern Russia. In fact, the surficial mode may be a source of Pd and other PGEs that is more abundant and easily refined, compared with the structurally bound mode.

Author Contributions: S.L. guided the study and interpretation of results, provided data handling, and organized the LA-ICP-MS analysis; V.T. formulated the problem and organized the research team; N.S. processed and rendered the ADSSC data; D.B. realized the hydrothermal experiment; I.P. realized the ETR-AAS study. All authors participated in writing the manuscript. All authors have read and agreed to the published version of the manuscript.

Funding: The research was performed within the framework of the state assignment for project No. 0284-2021-0002 and was partly funded by the Russian Foundation for Basic Research, grant No. 20-05-00142.

Data Availability Statement: No supporting data.

Acknowledgments: Taisa Pastushkova, Irina Voronova, and Vitaliy Menshikov are thanked for their assistance in the analytical studies. The cooperation with the scientists at the shared research centers “Isotope-geochemical Studies” of the Vinogradov Institute of Geochemistry SB RAS and “Ultra-microanalysis” of the Limnological Institute SB RAS are greatly appreciated. The authors would like to thank two anonymous reviewers for their valuable comments.

Conflicts of Interest: The authors declare no conflict of interest.

References

1. Bezmen, N.I.; Tikhomirova, V.I.; Kosogova, V.P. Pyrite-pyrrhotite geothermometer—Distribution of nickel and cobalt. *Geokhimiya* **1975**, *5*, 700–714. (In Russian)
2. Tauson, V.L. Isomorphism and endocrypty: Novel approaches in studies of behavior of microelements in mineral systems. *Geol. Geofiz.* **1999**, *40*, 1488–1494.
3. Vukmanovic, Z.; Reddy, S.M.; Godel, B.; Barnes, S.J.; Fiorentini, M.L.; Barnes, S.-J.; Kilburn, M.R. Relationship between microstructures and grain-scale trace element distribution in komatiite-hosted magmatic sulphide ores. *Lithos* **2014**, *184–187*, 42–61. [[CrossRef](#)]
4. Craig, J.R.; Vokes, F.M. The metamorphism of pyrite and pyritic ores: An overview. *Miner. Mag.* **1993**, *57*, 3–18. [[CrossRef](#)]
5. Tauson, V.L.; Lipko, S.V.; Arsent'ev, K.Y.; Smagunov, N.V. Crystal growth through the medium of nonautonomous phase: Implications for element partitioning in ore systems. *Crystallogr. Rep.* **2019**, *64*, 496–507. [[CrossRef](#)]
6. Schmidt, O.; Fazan, T.A.; Morais, J.; Fecher, G.H. Microanalysis of the surfaces of natural iron-based minerals by means of synchrotron radiation based experimental techniques. *Surf. Sci.* **2001**, *482–485*, 568–573. [[CrossRef](#)]
7. Tauson, V.L. The principle of continuity of phase formation at mineral surfaces. *Dokl. Earth Sci.* **2009**, *425*, 471–475. [[CrossRef](#)]
8. Walker, A.T.; Evans, K.A.; Kirkland, C.L. A novel application of image analysis to interpret trace element distribution in magmatic sulfides. *Lithos* **2020**, *362–363*, 105451. [[CrossRef](#)]

9. Tauson, V.L.; Akimov, V.V.; Parkhomenko, I.Y.; Nepomnyashchikh, K.V.; Men'shikov, V.I. A study of cadmium incorporation into pyrrhotites of various stoichiometries. *Geokhimiya* **2004**, *42*, 152–160.
10. Tauson, V.L.; Lipko, S.V.; Smagunov, N.V.; Kravtsova, R.G. Trace element partitioning dualism under mineral-fluid interaction: Origin and geochemical significance. *Minerals* **2018**, *8*, 282. [[CrossRef](#)]
11. Ikonnikova, N.Y.; Egorov, V.M.; Vasenin, A.R. Experimental PTFC diagrams of aqueous solutions of ammonium chloride. *Dokl. Akad. Nauk SSSR* **1970**, *192*, 407–409. (In Russian)
12. Tauson, V.L.; Bessarabova, O.I.; Kravtsova, R.G.; Pastushkova, T.M.; Smagunov, N.V. Determination of binding forms of gold in pyrite by means of statistical analysis. *Rus. Geol. Geophys.* **2001**, *43*, 56–64.
13. Tauson, V.L.; Babkin, D.N.; Akimov, V.V.; Lipko, S.V.; Smagunov, N.V.; Parkhomenko, I.Y. Trace elements as indicators of the physicochemical conditions of mineral formation in hydrothermal sulfide systems. *Rus. Geol. Geophys.* **2013**, *54*, 526–543. [[CrossRef](#)]
14. Tauson, V.L.; Lustenberg, E.E. Quantitative determination of modes of gold occurrence in minerals by the statistical analysis of analytical data samplings. *Geochem. Int.* **2008**, *46*, 423–428. [[CrossRef](#)]
15. Lipko, S.; Tauson, V.; Bychinskii, V. Gold partitioning in a model multiphase mineral-hydrothermal fluid system: Distribution coefficients, speciation and segregation. *Minerals* **2020**, *10*, 890. [[CrossRef](#)]
16. Tauson, V.L.; Parkhomenko, I.Y.; Babkin, D.N.; Men'shikov, V.I.; Lustenberg, E.E. Cadmium and mercury uptake by galena crystals under hydrothermal growth: A spectroscopic and element thermo-release atomic absorption study. *Eur. J. Mineral.* **2005**, *17*, 599–610. [[CrossRef](#)]
17. Tauson, V.L.; Lipko, S.V.; Arsent'ev, R.Y.; Mikhlin, Y.L.; Babkin, D.N.; Smagunov, N.V.; Pastushkova, T.M.; Voronova, I.Y.; Belozerova, O.Y. Dualistic distribution coefficients of trace elements in the system mineral-hydrothermal solution. IV. Platinum and silver in pyrite. *Geochem. Int.* **2017**, *55*, 753–774. [[CrossRef](#)]
18. Taylor, L.A. The system Ag-Fe-S: Phase equilibria and mineral assemblages. *Miner. Depos.* **1970**, *5*, 41–58. [[CrossRef](#)]
19. Palyanova, G.; Kokh, K.; Seryotkin, Y. Transformation of pyrite to pyrrhotite in the presence of Au-Ag alloys at 500 °C. *Am. Miner.* **2016**, *101*, 2731–2737. [[CrossRef](#)]
20. Pal'yanova, G.; Mikhlin, Y.; Kokh, K.; Karmanov, N. Experimental constraints on gold and silver solubility in iron sulfides. *J. Alloys Compd.* **2015**, *649*, 67–75. [[CrossRef](#)]
21. Makovicky, E.; Karup-Møller, S. The system Pd-Fe-S at 900°, 725°, 550°, and 400 °C. *Econ. Geol.* **1993**, *88*, 1269–1278. [[CrossRef](#)]
22. Ballhaus, C.; Ulmer, P. Platinum-group elements in the Merensky Reef: II. Experimental solubilities of platinum and palladium in Fe_{1-x}S from 950 to 450 °C under controlled *f*S₂ and *f*H₂. *Geochim. Cosmochim. Acta* **1995**, *59*, 4881–4888. [[CrossRef](#)]
23. Tauson, V.; Lipko, S.; Kravtsova, R.; Smagunov, N.; Belozerova, O.; Voronova, I. Distribution of “invisible” noble metals between pyrite and arsenopyrite exemplified by minerals coexisting in orogenic Au deposits of North-Eastern Russia. *Minerals* **2019**, *9*, 660. [[CrossRef](#)]
24. Skinner, B.J.; Luce, F.D. Solid solutions of the type (Ca, Mg, Mn, Fe)S and their use as geothermometers for the enstatite chondrites. *Am. Miner.* **1971**, *56*, 1269–1296.
25. Kravtsova, R.G.; Tauson, V.L.; Makshakov, A.S.; Bryansky, N.V.; Smagunov, N.V. Platinum group elements in arsenopyrites and pyrites of the Natakinskoe gold deposit (Northeastern Russia). *Minerals* **2020**, *10*, 318. [[CrossRef](#)]